Unexpected dependence of the anomalous Hall angle on the Hall conductivity in amorphous transition metal thin films

J. Karel,[1,2,*] D. S. Bouma,[3,4] C. Fuchs ,[4,5] S. Bennett,[1] P. Corbae ,[6] S. B. Song,[7]
B. H. Zhang,[7] R. Q. Wu,[8] and F. Hellman [3,4]

[1]*Department of Materials Science and Engineering, Monash University, Clayton, VIC 3800, Australia*
[2]*ARC Centre of Excellence in Future Low-Energy Electronics Technologies, Monash University, Clayton, VIC 3800, Australia*
[3]*Materials Science Division, Lawrence Berkeley National Lab, Berkeley, California 94720, USA*
[4]*Physics Department, University of California Berkeley, Berkeley, California 94720, USA*
[5]*Department of Physics and Astronomy, Julius-Maximilians-Universität, Würzburg 97074, Germany*
[6]*Department of Materials Science and Engineering, University of California Berkeley, Berkeley, California 94720, USA*
[7]*State Key Laboratory of Surface Physics, Key Laboratory of Computational Physical Sciences, and Department of Physics,
Fudan University, Shanghai 200433, China*
[8]*Department of Physics and Astronomy, University of California, Irvine, California 92697, USA*

The anomalous Hall effect (AHE), and magnetic and electronic transport properties were investigated in a series of amorphous transition metal thin films—Fe_xSi_{1-x}, Fe_xGe_{1-x}, Co_xGe_{1-x}, Co_xSi_{1-x}, and $Fe_{1-y}Co_ySi$. The experimental results are compared with density functional theory calculations of the density of Berry curvature and intrinsic anomalous Hall conductivity. In all samples, the longitudinal conductivity (σ_{xx}), magnetization (M), and Hall resistivity (ρ_{xy}) increase with increasing transition metal concentration; due to the structural disorder σ_{xx} is lower in all samples than a typical crystalline metal. In the systems with Fe as the transition metal (including $Fe_{1-y}Co_ySi$), the magnetization and AHE are large and in some cases greater than the crystalline analog. In all samples, the AHE is dominated by the intrinsic mechanism, arising from a nonzero, locally derived Berry curvature. The anomalous Hall angle (AHA) ($= \sigma_{xy}/\sigma_{xx}$) is as large as 5% at low temperature. These results are compared with the AHAs reported in a broad range of crystalline and amorphous materials. Previous work has shown that in a typical crystalline ferromagnet the Hall conductivity (σ_{xy}) and σ_{xx} are correlated and are usually either both large or both small, resulting in an AHA that decreases with increasing σ_{xy}. By contrast, the AHA increases linearly with increasing σ_{xy} in the amorphous systems. This trend is attributed to a generally low σ_{xx}, while σ_{xy} varies and can be large. In the amorphous systems, σ_{xx} and σ_{xy} are not coupled, and there may thus exist the potential to further increase the AHA by increasing σ_{xy}.

I. INTRODUCTION

The intrinsic contribution to the anomalous Hall effect (AHE) has attracted intense interest recently. This contribution is determined by the electronic structure of the material, and more specifically from the sum of the Berry phase over all occupied **k** states [1]. While the AHE typically occurs in ferromagnets, where it is expected to scale with the magnetization (M), it was discovered that a large AHE can arise due solely to a nonzero Berry curvature. The effect can be present in materials with little or no M, such as noncollinear antiferromagnets (Mn_3Ge, Mn_3Sn) or a low-M ferromagnetic kagome lattice ($Co_2Sn_2S_2$) [2–4]. Remarkably, two recent works found that the AHE in amorphous Fe_xSi_{1-x} and Fe_xGe_{1-x} thin films is also dominated by the intrinsic contribution, a surprising result in materials that lack long-range order (and thus **k** cannot be used to describe the system) [5,6]. This conclusion was based on the independence of the normalized Hall conduc-

tivity (σ_{xy}) from the longitudinal conductivity (σ_{xx}) as well as (in Fe_xGe_{1-x}) theoretical calculations of the intrinsic Hall conductivity determined from the density of Berry curvature [5,6]. The density of Berry curvature was calculated from the sum of local orbital states with spin-orbit correlation [5].

The physics of the AHE has been a topic of study for decades. In addition to the intrinsic mechanism, the transverse voltage under applied electric field and mutually perpendicular magnetic field can originate from one of two extrinsic contributions, skew scattering or side jump, which are both due to spin-dependent scattering from impurities with spin-orbit coupling [1]. A unified scaling theory has been developed to parse the individual contributions to the AHE [1,7]. More recently, there has been interest in using the AHE in a ferromagnet as a spin current source. The efficient generation of spin currents is critical to numerous low-energy electronic devices, including the attojoule logic gate [8] and spin-orbit torque magnetoresistive random access memory (SOT MRAM) [9]. When an electric field is applied in a ferromagnet, a transverse charge current and concomitant spin current are generated [10,11]. This spin current can be injected

*julie.karel@monash.edu

into an adjacent ferromagnetic layer, where it will produce a torque (spin transfer torque) on the spins. This effect was predicted and recently demonstrated experimentally [10,11]. The key advantage of using a FM as a spin current source is that the orientation of the injected spins points along the magnetization direction of the FM spin current source, which can be simply changed by changing the magnetization. This methodology offers the possibility to switch a perpendicular ferromagnetic layer [10,11]. By contrast, a common spin current source, the heavy metal in a heavy metal/ferromagnet (HM/FM) bilayer, can only efficiently switch an in-plane FM [10,12].

The potential to use the AHE to generate spin currents relies on the effect being large. The figure of merit used to quantify it is the anomalous Hall angle (AHA), which describes the efficiency of generating a transverse electric current from a longitudinal one [13]. It is given by the following equation, where σ_{xx} and σ_{xy} are the longitudinal and transverse conductivities, respectively.

$$\text{AHA} = \frac{\sigma_{xy}}{\sigma_{xx}}.$$

According to the unified scaling theory, σ_{xx} and σ_{xy} generally scale as $\sigma_{xy} \sim \sigma_{xx}^{\beta}$ where $\beta \geqslant 1$, and hence are either both large or both small for typical ferromagnets, resulting in a relatively small AHA [1,7]. Moreover, previous work has shown that the AHA normally decreases with increasing σ_{xy}, as might be expected from $\beta \geqslant 1$ [4]. There are notable exceptions to this trend of decreasing AHA with increasing σ_{xy}; materials such as GdPtBi, $Co_3Sn_2S_2$, and Co_2MnGa all exhibit a large AHA (as large as 20% in $Co_2Sn_2S_2$) [4,13,14]. In these cases, the topological properties in the electronic structure and resultant nonzero Berry curvature play an important role, causing large σ_{xy} despite small σ_{xx}. However, with the exception of Co_2MnGa, these large AHAs do not persist up to room temperature, a critical requirement for future spintronic applications. For instance, the largest reported AHA (20%) was found in $Co_2Sn_2S_2$ at 120 K [4]. At this temperature, σ_{xx} is reduced compared to 2 K due to electron-phonon scattering and σ_{xy} remains extraordinarily large due to the topological properties of the electronic structure.

In this work, the AHE and AHA are explored in a series of amorphous transition metal thin films. It will be shown that consistent with our earlier work on amorphous Fe_xSi_{1-x} and Fe_xGe_{1-x} systems, the AHE in all samples is dominated by the intrinsic mechanism, arising from a nonzero locally derived Berry curvature. We suggest these materials may enable future devices and explore one potential application, namely, spin current generation. It will be shown that the AHA can be engineered using disorder, which naturally reduces σ_{xx}, while M and σ_{xy} remain large and robust to disorder. Contrary to crystalline systems, the AHA increases with increasing σ_{xy} in a series of amorphous transition metal alloy thin films.

II. METHODS

A. Experiment

Amorphous thin films (70–1000 Å) of Fe_xSi_{1-x} ($x = 0.43$–0.71), Fe_xGe_{1-x} ($x = 0.45$–0.61), Co_xGe_{1-x} ($x = 0.45$–0.63), and $Fe_{1-y}Co_ySi$ ($y = 0, 0.1, 0.2, 0.3$) were

grown at room temperature by electron beam coevaporation of Fe, Si, Ge, and Co on amorphous SiN_x on Si substrates. Amorphous thin films of Co_xSi_{1-x} (800 Å, $x = 0.45$–0.73) were grown at room temperature on the aforementioned substrates by rf or dc magnetron sputtering from Si and Co targets, respectively. The composition ranges studied were selected in order to fabricate amorphous ferromagnetic films. All films were capped with 20 Å of Al or 30–50 Å of Al_2O_3 to prevent oxidation. The film compositions were verified using Rutherford backscattering spectrometry (RBS), with an estimated error no greater than ± 2 at. %. Although Fe and Co have similar masses, it was possible to distinguish and fit two separate peaks in the RBS spectra since the a-$Fe_{1-y}Co_ySi$ samples were relatively thin (70–100 Å). X-ray diffraction revealed no diffraction peaks (consistent with the amorphous structure). High-resolution transmission electron microscopy (HR TEM) has been previously performed to characterize the film structure (see Refs. [5,15–17] for representative images). An a-Fe_xSi_{1-x} thin film with $x = 0.55$ showed only a few small areas of poorly defined lattice fringes. Additionally, a selected area electron diffraction pattern measured using HR TEM from an $x = 0.61$ a-Fe_xGe_{1-x} sample (capped) showed a diffuse ring, as expected for an amorphous material. HR TEM has been performed on various capped and uncapped samples in cross section and uncapped samples in plan view, and consistently show amorphous films. These results, combined with the fact that Si and Ge are both well-known glass formers, indicates the samples in this study are amorphous. M as a function of applied magnetic field (H) was measured at various temperatures in a Quantum Design Magnetic Properties Measurement System (MPMS). a-Fe_xSi_{1-x}, a-$Fe_{1-y}Co_ySi$, and a-Co_xSi_{1-x} samples were patterned into a Hall bar using standard photolithography and wet etch techniques. These films were etched in a dilute mixture of hydrofluoric and nitric acid (400 ml H_2O : 2 ml HNO_3 : 1 ml HF); the etching time depends on the composition and ranged from 30 s–4 min for these 70–1000 Å thick films. The a-Fe_xGe_{1-x} and a-Co_xGe_{1-x} samples were measured using the van der Pauw method [18]. For all measurements, contacts were made using indium solder. Temperature- and H-dependent longitudinal (ρ_{xx}) and transverse resistivity (ρ_{xy}) measurements were carried out using an ac lock-in technique with currents below 2 μA and frequencies below 17 Hz in either a Quantum Design Physical Properties Measurement System (PPMS) or Magnetic Properties Measurement System (MPMS). Some of our a-Fe_xSi_{1-x} ($x = 0.48, 0.55, 0.67, 0.71$) and a-Fe_xGe_{1-x} ($x = 0.45, 0.48, 0.54, 0.61$) results have been previously reported [5,6].

B. Density functional theory calculations

Density functional theory (DFT) calculations were performed using the projector augmented wave (PAW) [19,20] formalism as implemented in the Vienna *ab initio* simulation package (VASP) [21,22]. The exchange-correlation interaction among electrons is described within the framework of the spin-polarized generalized gradient approximation (GGA) with the Perdew-Burke- Ernzerhof functional [23]. To obtain an amorphous Fe_xSi_{1-x} ($x = 0.50$) structure, five different

configurations were built by randomly placing equal amounts of Fe and Si atoms in a $4 \times 4 \times 4$ supercell with 128 sites. They were heated up to 3000 K in 10 ps, melted at 3000 K for 4 ps, and cooled down to 100 K in 6 ps through *ab initio* molecular dynamics (AIMD) simulations under the canonical ensemble condition. Further structural relaxation was carried out until the force on each atom became less than 0.01 eV/Å. The intrinsic anomalous Hall conductivity (AHC) was calculated for each structure by integrating the Berry curvature over the Brillouin zone, which is, in this case, the entire supercell [24]. The Boltzmann average of the AHC of the five supercell configurations was then calculated at 300 K. The large supercell used here results in a very small Brillouin zone; however, this approach is justified since spin-orbit coupling information in electronic states is preserved regardless of the number of times the Brillouin zone is folded [24]. Only the Γ point was used during the AIMD simulations; a $3 \times 3 \times 3$ Monkhorst-Pack k-point mesh was adopted for geometry optimization, and a $5 \times 5 \times 5$ k-point mesh was used for the AHE calculation.

III. RESULTS AND DISCUSSION

Figure 1(a) shows the longitudinal resistivity (ρ_{xx}) as a function of temperature for the a-Fe$_{1-y}$Co$_y$Si samples investigated in this work. The nominal compositions for this series are $y = 0$, 0.1, 0.2, 0.3, while the experimentally determined compositions are given in the legend. In contrast to the behavior of a typical crystalline metal, ρ_{xx} is not strongly temperature dependent in any of the samples. Similar temperature dependence of the resistivity was observed for all samples investigated in this study. This behavior is consistent with what is expected in disordered materials where the mean free path is on the order of an interatomic spacing and therefore temperature independent [25,26]. The longitudinal resistivity in Fig 1(a) appears to be primarily driven by the total concentration of transition metal (with respect to Si), which increases from 0.57 to 0.62, as the resistivity decreases. The two samples with the lowest resistivity have the same total concentration of transition metal (0.62). Within this sample set, the one with the greatest Co content has a slightly lower resistivity, although the difference may not be large enough to be significant. Figure 1(b) shows the longitudinal conductivity as a function of transition metal concentration for all of the amorphous thin films. Consistent with the a-Fe$_{1-y}$Co$_y$Si results, the longitudinal conductivity increases with increasing transition metal content in all of the systems probed here. The very short mean free path does not change significantly, due to the amorphous structure, indicating the longitudinal conductivity primarily depends on a change in carrier concentration.

Figure 2 displays the saturation magnetization (M_s) versus transition metal content for the amorphous thin films as indicated, and the inset shows a representative hysteresis loop with the magnetic field applied in the plane of the film for amorphous Fe$_{0.44}$Co$_{0.18}$Si$_{0.38}$ at 2 and 300 K. There is a clear distinction between the amorphous systems containing primarily Fe (including a-Fe$_{1-y}$Co$_y$Si) and those that contain mainly Co. In the Fe systems, the samples are still weakly ferromagnetic near $x = 0.45$; previous work has shown that magnetism occurs at $x \sim 0.40$ [27]. When $x \geqslant$
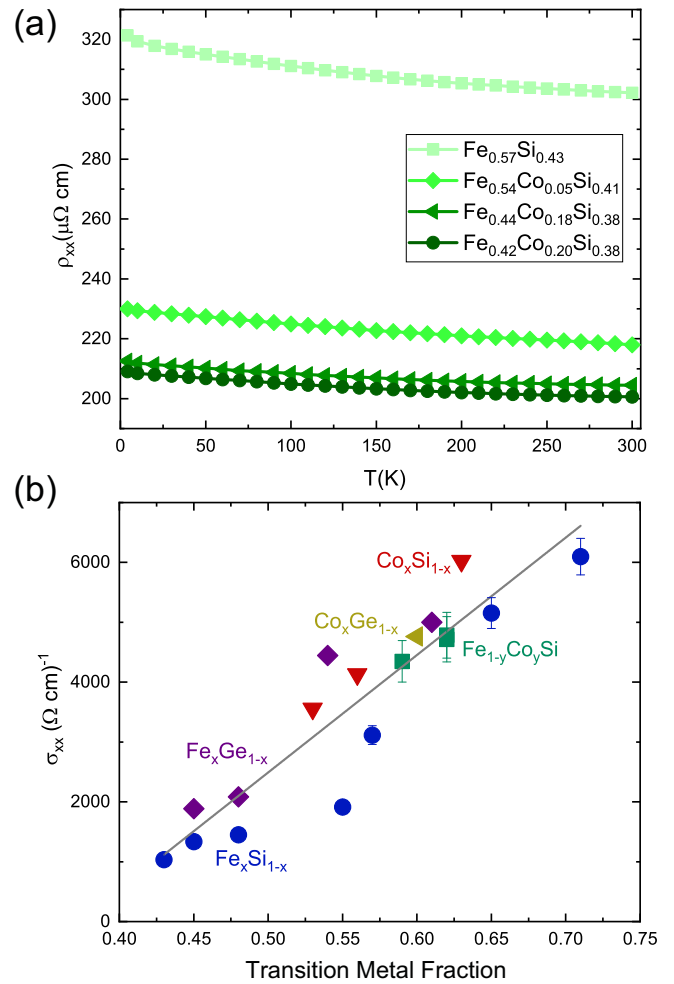

FIG. 1. (a) Longitudinal resistivity (ρ_{xx}) as a function of temperature for a series of amorphous Fe$_y$Co$_{1-y}$Si thin films. The compositions listed are experimentally determined from RBS and correspond from top to bottom to the nominal compositions $y = 0$, 0.1, 0.2, 0.3. (b) Longitudinal conductivity (σ_{xx}) at low temperature (2–4.2 K) as a function of transition metal concentration for all samples, as indicated. The line is a guide to the eye, and representative error bars are shown. Amorphous Fe$_x$Si$_{1-x}$ and Fe$_x$Ge$_{1-x}$ data adapted from Refs. [5,6], respectively. Each material system in (b) is represented by a different symbol: Fe$_x$Si$_{1-x}$ (blue circle), Fe$_x$Ge$_{1-x}$ (purple diamond), Co$_x$Ge$_{1-x}$ (gold left-pointing triangle), Co$_x$Si$_{1-x}$ (red down-pointing triangle), and Fe$_{1-y}$Co$_y$Si (green square).

0.55, the materials are ferromagnetic at room temperature [5,6,16]. M_s increases with increasing Fe content, which can be understood as simply due to an increase in the number of Fe-Fe first nearest neighbors [5,16]. Previous work has found that the magnetization is enhanced in amorphous Fe$_x$Si$_{1-x}$ thin films in comparison to crystalline thin films with the same composition [16]. This enhancement was attributed to a reduction in the number of Fe-Si first nearest neighbor pairs in the amorphous material, which reduced p-d orbital hybridization, leading to an enhanced moment. The magnetization of bulk crystalline Fe$_{0.45}$Co$_{0.05}$Si$_{0.50}$ at 5 K is approximately 2 emu/cm^3 [28]. Although a comparable amorphous composition was not obtained, the trend in the data
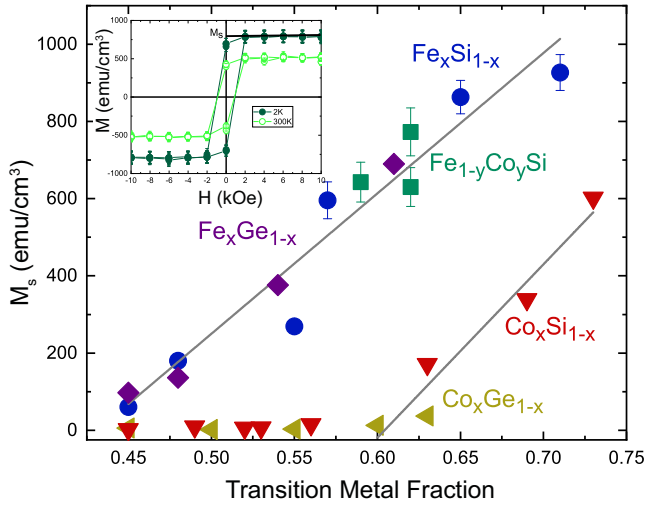
FIG. 2. Saturation magnetization (M_s) at 2 K as a function of transition metal content in a series of amorphous thin films. M_s is the value of M at high H (well above the coercive field) extrapolated to $H = 0$, as shown in the inset. The amorphous Fe_xSi_{1-x} and Fe_xGe_{1-x} data were reported in Refs. [5,6]. The two lines, one for the Fe-based compounds and the other for the Co-based systems, are a guide to the eye. Representative error bars are shown. Each material system is represented by a different symbol: Fe_xSi_{1-x} (blue circle), Fe_xGe_{1-x} (purple diamond), Co_xGe_{1-x} (gold left-pointing triangle), Co_xSi_{1-x} (red down-pointing triangle) and $Fe_{1-y}Co_ySi$ (green square). The inset shows a representative $M(H)$ curve for $Fe_{0.44}Co_{0.18}Si_{0.38}$ with H applied in the plane of the film for 2 and 300 K, as indicated.

seems to indicate a similar enhancement may be present in the amorphous $Fe_{1-y}Co_ySi$ system. In contrast to the Fe-rich materials, the amorphous thin films containing mainly Co do not present appreciable magnetization until $x > 0.60$. The difference in transition metal concentration where ferromagnetism is present (0.60 for Co-based systems versus 0.40 for Fe-based systems) can be understood by considering a simple interaction-based model introduced by Jaccarino and Walker, which only accounts for first nearest neighbor direct exchange interactions [29]. The simple model predicts a minimum number of ferromagnetic transition metal neighbors necessary to achieve a significant magnetic moment in the material; this minimum number is greater for Co than for Fe, explaining the difference in transition metal concentration where appreciable magnetization is observed [30,31].

Figure 3(a) displays representative ρ_{xy} versus H curves at various temperatures for a-$Fe_{0.42}Co_{0.20}Si_{0.38}$. The inset shows normalized ρ_{xy} and out-of-plane magnetization (M_z) versus H for the same sample, indicating the Hall resistivity scales with the magnetization. The primary charge carriers are holes for the a-Fe_xSi_{1-x}, a-Fe_xGe_{1-x}, a-Co_xSi_{1-x}, and a-$Fe_{1-y}Co_ySi$ systems, and the primary charge carriers are electrons in the a-Co_xGe_{1-x} thin films. For all these material systems, the carrier concentrations extracted from a simple two-band model at high temperature ($\geqslant 4.2$ K) yielded unphysical results, indicating a multiband system, where each band has separate mobilities and Hall coefficients. At low temperatures, with reduced thermal broadening of the Fermi function, the band structure could generally be approximated by a two-band
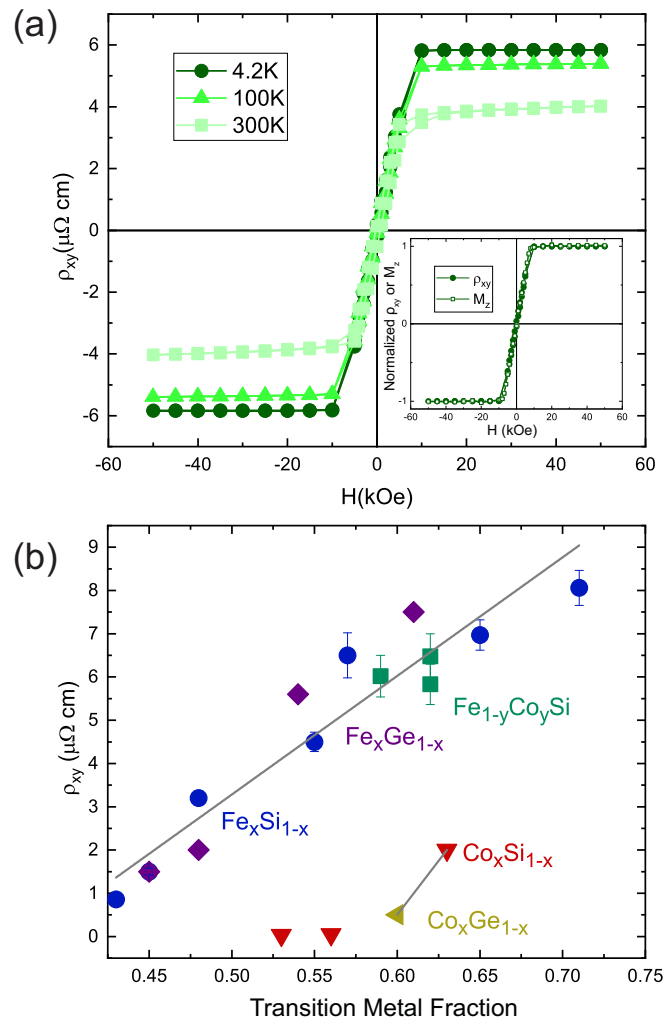

FIG. 3. (a) A representative curve of ρ_{xy} versus H for an a-$Fe_{0.42}Co_{0.20}Si_{0.38}$ thin film at various temperatures, as indicated. The inset shows normalized ρ_{xy} and out-of-plane magnetization (M_z) versus H for the same sample, indicating the Hall resistivity scales with the magnetization. (b) Transverse resistivity (ρ_{xy}) versus transition metal content for amorphous thin films at low temperature (2– 4.2 K). For all samples, these data are determined by extrapolating the high-field slope of ρ_{xy} versus H [as shown in (a)] to $H = 0$. Data from amorphous Fe_xSi_{1-x} and Fe_xGe_{1-x} are from Refs. [5,6]. The two lines, one for the Fe-based compounds and the other for the Co-based systems, are a guide to the eye. Representative error bars are shown in (b). Each material system is represented by a different symbol: Fe_xSi_{1-x} (blue circle), Fe_xGe_{1-x} (purple diamond), Co_xGe_{1-x} (gold left-pointing triangle), Co_xSi_{1-x} (red down-pointing triangle), and $Fe_{1-y}Co_ySi$ (green square).

system, assuming a free electron model with the mean free path on the order of an interatomic spacing. The error bars introduced in extracting the Hall coefficient from an iterative fit were too large to meaningfully determine the composition dependence of the carrier concentration within a material system in a-Co_xSi_{1-x}, a-$Fe_{1-y}Co_ySi$, or a-Co_xGe_{1-x}. We fit our experimental data to a calculated curve, which contains the ordinary Hall effect contribution ($R_0 H$) and the anomalous Hall effect component ($R_s M_z$), where R_0 and R_s are both
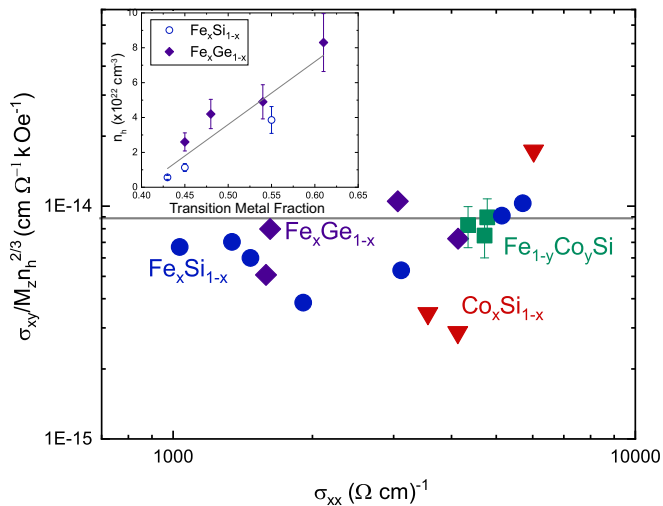
FIG. 4. Hall conductivity (σ_{xy}) normalized by M_z and $n_h^{2/3}$ versus longitudinal conductivity (σ_{xx}) for the amorphous samples studied in this work at low temperature (2–4.2 K). a-Co_xGe_{1-x} is not shown since a meaningful carrier concentration could not be determined for $x = 0.60$, which was the only sample in the series exhibiting an AHE. Data from amorphous Fe_xSi_{1-x} and Fe_xGe_{1-x} are from Refs. [5,6]. Each material system is represented by a different symbol: Fe_xSi_{1-x} (blue circles), Fe_xGe_{1-x} (purple diamonds), Co_xSi_{1-x} (red inverted triangles), and $Fe_{1-y}Co_ySi$ (green squares). Representative error bars are shown on the $Fe_{1-y}Co_ySi$ data. The inset shows the composition dependence of the carrier concentration for a-Fe_xSi_{1-x} and a-Fe_xGe_{1-x}. For samples with $x > 0.60$, $\delta\rho_{xy}/\delta H$ is too small to measure. Thus, for a-Co_xSi_{1-x}, a-$Fe_{1-y}Co_ySi$, and a-Fe_xSi_{1-x} ($x > 0.60$), the carrier concentration was approximated based on the composition dependence shown in the inset.

fitting parameters and are the ordinary and anomalous Hall coefficients, respectively. The large error bars in the iterative fit arise because M_z is the experimental out-of-plane magnetization, and experimental noise in this curve therefore introduces uncertainty into the iterative fit. Note that the Hall effect measurements have only been conducted on the ferromagnetic samples in this work. In a-Fe_xSi_{1-x} and a-Fe_xGe_{1-x}, the carrier concentration increased from 0.05 to 8×10^{22} cm^{-3} with increasing x (Fig. 4 inset); the carrier concentrations of a-Fe_xSi_{1-x} and a-Fe_xGe_{1-x} are remarkably similar given the differences in size of Si and Ge. In the scaling analysis (discussed later), we have approximated the concentration dependence of the carrier concentration in a-Co_xSi_{1-x} and a-$Fe_{1-y}Co_ySi$ based on the dependence of a-Fe_xSi_{1-x} and a-Fe_xGe_{1-x} shown in the inset of Fig. 4, an approach which is justified by the linear dependence of the longitudinal conductivity on transition metal fraction.

The transverse resistivity (ρ_{xy}) as a function of transition metal content is shown in Fig. 3(b) for the amorphous thin films studied in this work. Consistent with the M_s trends, ρ_{xy} increases with increasing transition metal content. Amorphous Co_xGe_{1-x} and Co_xSi_{1-x} begin to display an AHE at the same composition as that at which the magnetization becomes appreciable. In the a-$Fe_{1-y}Co_ySi$ system, increasing the Co content (and consequently reducing the Fe content) does not appear to play as important a role as the total transition metal

concentration. The Fe compounds (including a-$Fe_{1-y}Co_ySi$) present a large AHE that persists up to room temperature (for transition metal content greater than or equal to 0.55). It has been previously found that the AHE is larger in amorphous Fe_xSi_{1-x} thin films than crystalline thin films with an analogous composition [6].

To understand the origin of the large AHE in these amorphous transition metal thin films, the data can be examined within the context of the unified scaling theory [1,7]. This theory suggests plotting the anomalous Hall conductivity (σ_{xy}) versus the longitudinal conductivity (σ_{xx}), where $\sigma_{xy} \sim \rho_{xy}/\rho_{xx}^2$. This naturally gives rise to three different scaling regimes based on the longitudinal conductivity. In the clean limit, (e.g., $\sigma_{xx} > 10^6\ \Omega^{-1}\,cm^{-1}$), the theory predicts and experiments have verified that $\sigma_{xy} \propto \sigma_{xx}$, indicating skew scattering is the primary contribution to the AHE in this conductivity region. In the intermediate conductivity range, $10^4\ \Omega^{-1}\,cm^{-1} < \sigma_{xx} < 10^6\ \Omega^{-1}\,cm^{-1}$, theory predicts σ_{xy} is independent of σ_{xx}, meaning the intrinsic mechanism, arising from a nonzero Berry curvature in the electronic structure, is typically dominant. The low-conductivity range ($\sigma_{xx} < 10^4\ \Omega^{-1}\,cm^{-1}$) is not fully understood. Empirical results have suggested the scaling is $\sigma_{xy} \propto \sigma_{xx}^{\gamma}$ with $\gamma = 1.6$–1.8, and calculations based on phonon-assisted hopping and percolation theory in systems where $\sigma_{xx} < 10^2\ \Omega^{-1}\,cm^{-1}$ have shown scaling of $1.33 \leqslant \gamma \leqslant 1.76$ [7,32]. Our previous experimental studies in the low-σ_{xx} regime on amorphous Fe_xSi_{1-x} and Fe_xGe_{1-x} have found that σ_{xy}, when suitably normalized by the out-of-plane magnetization (M_z) and the number of charge carriers, is independent of σ_{xx}, suggesting the intrinsic mechanism plays a crucial role in the low-conductivity region as well [5,6]. This result is surprising since the conventional definition of the Berry curvature is formulated using **k**, which is no longer a good quantum number in an amorphous system. Nevertheless, through DFT calculations of the density of Berry curvature, which is determined by the sum of spin-orbit correlations of the local orbitals, the a-Fe_xGe_{1-x} work showed unambiguously that the intrinsic mechanism still remains in a material lacking a well-defined band structure [5].

In accordance with the unified scaling theory, Fig. 4 shows $\sigma_{xy}/M_z n_h^{2/3}$ versus σ_{xx} for amorphous $Fe_{1-y}Co_ySi$, Fe_xSi_{1-x}, Fe_xGe_{1-x}, and Co_xSi_{1-x} thin films [5,6]. Generally, the unified scaling theory suggests plotting σ_{xy} versus σ_{xx}, resulting in the scaling $\sigma_{xy} \propto \sigma_{xx}^{\gamma}$ with $\gamma = 2.39$ for these data, which is not consistent with the previously predicted mechanisms discussed above. However, following previous work [5,6], it is necessary to account for changes in the magnetization and carrier concentration by normalizing σ_{xy} by M_z and $n_h^{2/3}$, for the following reasons. The unified scaling theory was developed based on a change in carrier lifetime, and plotting σ_{xx} represents this change in carrier lifetime [1,7]. The temperature-dependent resistivity data in Fig. 1(a) shows, however, that the carrier concentration is the primary factor driving a change in resistivity between samples. Moreover, the magnetization is not accounted for in the unified scaling theory. When normalized, $\sigma_{xy}/M_z n_h^{2/3}$ is independent of σ_{xx}, indicating the AHE is driven by the intrinsic mechanism. We note that the side-jump mechanism could produce a similar scaling. However, DFT calculations showed that the intrinsic mechanism is the primary contribution to the AHE in

amorphous Fe_xGe_{1-x}, and the side-jump mechanism comprised only a small composition-independent contribution [5].

To quantitatively probe the intrinsic contribution, we have performed DFT calculations on an amorphous supercell of Fe_xSi_{1-x} to extract a density of Berry curvature and the intrinsic anomalous Hall conductivity for $x = 0.50$. We find $\sigma_{xy}^{int} = 28\,(\Omega\,cm)^{-1}$, compared to experimental total Hall conductivities of $\sigma_{xy}^{total} = 17\,(\Omega\,cm)^{-1}$ and $43\,(\Omega\,cm)^{-1}$ for $x = 0.55$ and 0.57, respectively. It is important to note that the calculated nonzero density of Berry curvature is clear evidence of the intrinsic contribution; the calculations do not include the side-jump or skew-scattering mechanisms. The similarity between the calculated intrinsic Hall conductivity and the experimental total Hall conductivities, particularly when accounting for the difference in composition, suggests the AHE is dominated by the intrinsic effect in amorphous Fe_xSi_{1-x}, with the side-jump mechanism comprising a minor contribution. Based on these representative calculations, the previous amorphous Fe_xGe_{1-x} work [5] and the independence of $\sigma_{xy}/M_z n_h^{2/3}$ on σ_{xx} for all samples, we suggest the intrinsic contribution dominates in all amorphous transition metal thin films studied here. These results suggest that local topology in the electronic structure might also be exploited in amorphous materials.

We now turn to the anomalous Hall angle. Figure 5(a) displays the AHA plotted against σ_{xy} for earlier work on crystalline materials. The gray line is a guide to the eye which depicts a trend of decreasing AHA as σ_{xy} increases, as previously reported [4]. This result in typical ferromagnets is described by the unified scaling theory, where σ_{xy} and σ_{xx} are correlated and are either both large or both small [1,7]. Therefore as σ_{xy} increases, σ_{xx} also does, leading to a decrease in the AHA. Figure 5(b) shows the AHA versus σ_{xy} from this (filled data points) and previous studies of amorphous materials (open data points). These data follow an entirely different trend. The AHA increases linearly with increasing σ_{xy}, indicating it primarily depends on the Hall conductivity. Further confirming this point, Fig. 5(c) shows a plot of AHA versus σ_{xx} for the amorphous samples studied in this work. If the AHA depended substantially on σ_{xx}, it should decrease with increasing σ_{xx}, which it clearly does not.

Based on the AHA results observed in amorphous materials, σ_{xy} and σ_{xx} evidently can be decoupled, meaning both are not necessarily either large or small. In general, the lack of temperature dependence of the longitudinal resistivity indicates the mean free path of a charge carrier is on the order of an interatomic spacing, resulting in a low σ_{xx} in the disordered amorphous systems. In contrast, the magnetization and Hall conductivity are robust to disorder and can remain high, as large as or larger than in a comparable crystalline system. Hence, the AHA increases with increasing σ_{xy}. In the samples studied, the AHA was as large as $\sim$5%, a reasonably large value even in comparison to crystalline ferromagnets [as observed in Fig. 5(a)]. The intrinsic mechanism of the AHE has been generally considered to only be present in crystalline systems, while here it has been shown to dominate in fully disordered materials, resulting in an AHA of the same magnitude. What is more, the amorphous systems may have the potential to increase the AHA further by increasing σ_{xy} without substantially changing σ_{xx}. This could be realized by increasing M through the addition of a magnetic rare-
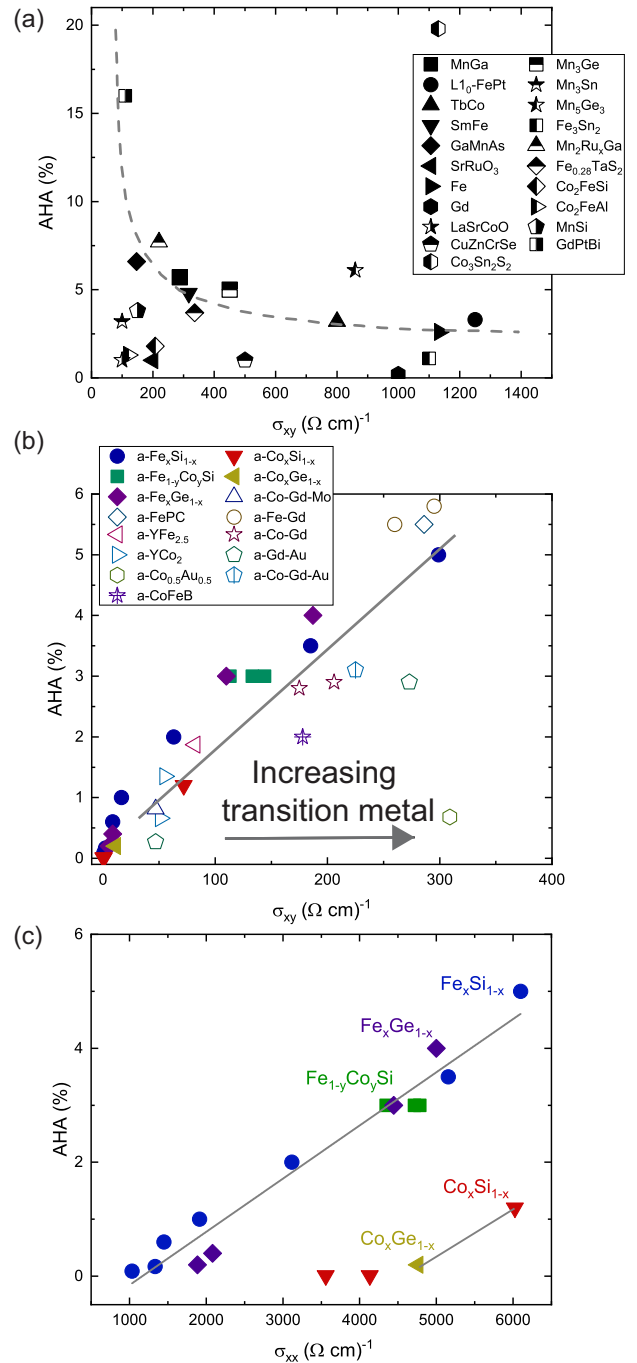

FIG. 5. AHA versus Hall conductivity for (a) crystalline materials and (b) amorphous materials; and (c) AHA versus longitudinal conductivity for the amorphous materials in this work. The data and gray dashed line (guide to the eye) in (a) are based on Ref. [4]. The solid line in (b) is a linear fit to the data. In (b), closed symbols are data from this work (at 2–4.2 K), and open symbols are literature values (at 50–77 K). The gray lines in (c) are a guide to the eye. Data points were taken from the following references: Co₃Sn₂S₂ [4], MnGa [33], $L1_0$-FePt [34], TbCo [35], SmFe [36], GaMnAs [37], SrRuO₃ [38], Fe [39], Gd [39], LaSrCoO [39], CuZnCrSe [39], Mn₃Ge [2], Mn₃Sn [3], Mn₅Ge₃ [40], Fe₃Sn₂ [14], Mn₂RuₓGa [41], Fe₀.₂₈TaS₂ [42], Co₂FeSi [43], Co₂FeAl [43], MnSi [28], *a*-FePC [44], *a*-YFe₂.₅ [44], *a*-YCo₂ [44], *a*-Co₀.₅Au₀.₅ [44], *a*-CoFeB [45], *a*-Co-Gd-Mo [44], *a*-Fe-Gd [44], *a*-Co-Gd [44], *a*-Gd-Au [44], *a*-Co-Gd-Au [44], and GdPtBi [14].

earth element or introducing an element with large spin-orbit coupling to generate a larger nonzero Berry curvature. Such a methodology is not available in crystalline systems as an increase in σ_{xy} will typically result in an increase in σ_{xx}, and thus a decrease in the AHA.

IV. CONCLUSION

The magnetic, electronic, and magnetotransport properties in a series of amorphous transition metal thin films (Fe$_x$Si$_{1-x}$, Fe$_x$Ge$_{1-x}$, Co$_x$Ge$_{1-x}$, Co$_x$Si$_{1-x}$, and Fe$_{1-y}$Co$_y$Si) were studied. M, σ_{xx}, and ρ_{xy} all increase with increasing transition metal content, and the systems containing predominantly Fe exhibit a large M and AHE that persists up to room temperature for $x \geqslant 0.55$. An analysis of the scaling of σ_{xy} and theoretical calculations revealed that the AHE in all samples is driven primarily by the intrinsic mechanism resulting from a nonzero locally derived Berry curvature, explained quantitatively by the DFT-derived density of curvature in these amorphous materials. The AHA is as large as 5%, and an examination of amorphous materials reveals that the AHA increases with increasing σ_{xy}, contrary to the trend found in crystalline systems. The reason for this trend is that the longitudinal conductivity is low in amorphous systems, while the magnetization and consequently σ_{xy} are robust to disorder and can therefore be large. These results indicate that amorphous transition metal alloys may be a promising material system for use as a spin current generator in future spintronic applications.

[1] N. Nagaosa, J. Sinova, S. Onoda, A. H. MacDonald, and N. P. Ong, Rev. Mod. Phys. **82**, 1539 (2010).

[2] A. K. Nayak, J. E. Fischer, Y. Sun, B. Yan, J. Karel, A. C. Komarek, C. Shekhar, N. Kumar, W. Schnelle, J. Kuebler, C. Felser, and S. S. P. Parkin, Sci. Adv. **2**, e1501870 (2016).

[3] S. Nakatsuji, N. Kiyohara, and T. Higo, Nature **527**, 212 (2015).

[4] E. Liu, Y. Sun, N. Kumar, L. Muechler, A. Sun, L. Jiao, S-Y. Yang, D. Liu, A. Liang, Q. Xu, J. Kroder, V. Suess, H. Borrmann, C. Shekhar, Z. Wang, C. Xi, W. Wang, W. Schnelle, S. Wirth, Y. Chen *et al.*, Nat. Phys. **14**, 1125 (2018).

[5] D. S. Bouma, Z. Chen, B. Zhang, F. Bruni, M. E. Flatte, A. Ceballos, R. Streubel, L.-W. Wang, R. Q. Wu, and F. Hellman, Phys. Rev. B **101**, 014402 (2020).

[6] J. Karel, C. Bordel, D. S. Bouma, A. de Lorimier-Farmer, H. J. Lee, and F. Hellman, Europhys. Lett. **114**, 57004 (2016).

[7] S. Onoda, N. Sugimoto, and N. Nagaosa, Phys. Rev. Lett. **97**, 126602 (2006).

[8] S. Manipatruni, D. E. Nikonov, and I. A. Young, Nat. Phys. **14**, 338 (2018).

[9] J. Kim, A. Paul, P. A. Crowell, S. J. Koester, S. S. Sapatnekar, J.-P. Wang, and C. H. Kim, Proc. IEEE **103**, 106 (2015).

[10] T. Taniguchi, J. Grollier, and M. D. Stiles, Phys. Rev. Appl. **3**, 044001 (2015).

[11] S. Iihama, T. Taniguchi, K. Yakushiji, A. Fukushima, Y. Shiota, S. Tsunegi, R. Hiramatsu, S. Yuasa, Y. Suzuki, and H. Kubota, Nat. Electron. **1**, 120 (2018).

[12] T. Wang, J. Q. Xiao, and X. Fan, Spin **7**, 1740013 (2017).

[13] A. Markou, D. Kriegner, J. Gayles, L. Zhang, Y-C. Chen, B. Ernst, Y. H Lai, W. Schnelle, Y-H. Chu, Y. Sun, and C. Felser, Phys Rev B **100**, 054422 (2019).

[14] T. Suzuki, R. Chisnell, A. Devarakonda, Y.-T. Liu, W. Feng, D. Xiao, J. W. Lynn, and J. G. Checkelsky, Nat. Phys. **12**, 1119 (2016).

[15] A. X. Gray, J. Karel, J. Minár, C. Bordel, H. Ebert, J. Braun, S. Ueda, Y. Yamashita, L. Ouyang, D. J. Smith, K. Kobayashi, F. Hellman, and C. S. Fadley, Phys. Rev. B **83**, 195112 (2011).

[16] J. Karel, Y. N. Zhang, C. Bordel, K. H. Stone, T. Y. Chen, C. A. Jenkins, D. J. Smith, J. Hu, R. Q. Wu, S. M. Heald, J. B. Kortright, and F. Hellman, Mater. Res. Express **1**, 026102 (2014).

[17] J. Karel, D. S. Bouma, J. Martinez, Y. N. Zhang, J. A. Gifford, J. Zhang, G. J. Zhao, D. R. Kim, B. C. Li, Z. Y. Huang, R. Q. Wu, T. Y. Chen, and F. Hellman, Phys. Rev. Mater. **2**, 064411 (2018).

[18] L. J. van der Pauw, Phillips Res. Rep. **13**, 1 (1958).

[19] P. E. Blöchl, Phys. Rev. B **50**, 17953 (1994).

[20] G. Kresse and D. Joubert, Phys. Rev. B **59**, 1758 (1999).

[21] G. Kresse and J. Hafner, Phys. Rev. B **47**, 558 (1993).

[22] G. Kresse and J. Furthmüller, Phys. Rev. B **54**, 11169 (1996).

[23] J. P. Perdew, K. Burke, and M. Ernzerhof, Phys. Rev. Lett. **77**, 3865 (1996).

[24] B. H. Zhang, Z. Wang, Y. N. Zhang, and R. Q. Wu, Phys. Rev. Mater. **3**, 095602 (2019).

[25] J. H. Mooij, Phys. Status Solidi A **17**, 521 (1973).

[26] C. C. Tsuei, Phys. Rev. Lett. **57**, 1943 (1986).

[27] Ph. Mangin and G. Marchal, J. Appl. Phys. **49**, 1709 (1978).

[28] N. Manyala, Y. Sidis, J. F. DiTusa, G. Aeppli, D. P. Young, and Z. Fisk, Nat. Mater. **3**, 255 (2004).

[29] V. Jaccarino and L. R. Walker, Phys. Rev. Lett. **15**, 258 (1965).

[30] K. Buschow, M. Brouha, J. Biesterbos, and A. Dirks, Physica B+C (Amsterdam) **91**, 261, (1977).

[31] J. Chappert, R. Arrese-Boggiano, and J. M. D. Coey, J. Magn. Magn. Mater. **7**, 175 (1978).

[32] X.-J. Liu, X. Liu, and J. Sinova, Phys. Rev. B **84**, 165304 (2011).

[33] F. Wu, E. P. Sajitha, S. Mizukami, D. Watanabe, T. Miyazaki, H. Naganuma, M. Oogane, and Y. Ando, Appl. Phys. Lett. **96**, 042505 (2010).

[34] J. Yu, U. Ruediger, A. D. Kent, R. F. C. Farrow, R. F. Marks, D. Weller, L. Folks, and S. S. P. Parkin, J. Appl. Phys. **87**, 6854 (2000).

[35] T. W. Kim and R. J. Gambino, J. Appl. Phys. **87**, 1869 (2000).

[36] T. W. Kim, S. H. Lim, and R. J. Gambino, J. Appl. Phys. **89**, 7212 (2001).

[37] Y. Pu, D. Chiba, F. Matsukura, H. Ohno, and J. Shi, Phys. Rev. Lett. **101**, 117208 (2008).

[38] Z. Fang, N. Nagaosa, K. S. Takahashi, A. Asamitsu, R. Mathieu, T. Ogasawara, H. Yamada, M. Kawasaki, Y. Tokura, and K. Terakura, Science **302**, 92 (2003).

[39] T. Miyasato, N. Abe, T. Fujii, A. Asamitsu, S. Onoda, Y. Onose, N. Nagaosa, and Y. Tokura, Phys. Rev. Lett. **99**, 086602 (2007).

[40] C. Zeng, Y. Yao, Q. Niu, and H. H. Weitering, Phys. Rev. Lett. **96**, 037204 (2006).

[41] N. Thiyagarajah, Y.-C. Lau, D. Betto, K. Borisov, J. M. D. Coey, P. Stamenov, and K. Rode, Appl. Phys. Lett. **106**, 122402 (2015).

[42] J. Dijkstra, P. J. Zijlema, C. F. V. Bruggen, C. Haas, and R. A. D. Groot, J. Phys.: Condens. Matter **1**, 6363 (1989).

[43] I. M. Imort, P. Thomas, G. Reiss, and A. Thomas, J. Appl. Phys. **111**, 07D313 (2012).

[44] T. R. McGuire, R. J. Gambino, and R. C. Taylor, J. Appl. Phys. **48**, 2965 (1977).

[45] G. Su, Y. Li, D. Hou, X. Jin, H. Liu, and S. Wang, Phys. Rev. B **90**, 214410 (2014).